Tellus SERIES B CHEMICAL AND PHYSICAL METEOROLOGY
PUBLISHED BY THE INTERNATIONAL METEOROLOGICAL INSTITUTE IN STOCKHOLM

Tellus (2011), 63B, 751–769
Printed in Singapore. All rights reserved

TELLUS

Thermal IR radiative properties of mixed mineral dust and biomass aerosol during SAMUM-2

By CLAAS H. KÖHLER[1]*, THOMAS TRAUTMANN[1], ERWIN LINDERMEIR[1], WILLEM VREELING[2], KIRSTEN LIEKE[3], KONRAD KANDLER[3], BERNADETT WEINZIERL[4], SILKE GROß[5], MATTHIAS TESCHE[6] and MANFRED WENDISCH[7], [1]*Deutsches Zentrum für Luft- und Raumfahrt (DLR), Institut für Methodik der Fernerkundung, 82234 Oberpfaffenhofen, Germany;* [2]*Netherlands Institute for Space Research (SRON), Landleven 12, 9747 AD Groningen, Netherlands;* [3]*Institut für Angewandte Geowissenschaften, Technische Universität Darmstadt, Schnittspahnstr. 9, 64287 Darmstadt, Germany;* [4]*Deutsches Zentrum für Luft- und Raumfahrt (DLR), Institut für Physik der Atmosphäre, 82234 Oberpfaffenhofen, Germany;* [5]*Ludwig-Maximilians-Universität München, Meteorologisches Institut, Theresienstr. 37, 80333 München, Germany;* [6]*Leibniz-Institut für Troposphärenforschung (IfT), Permoserstr. 15, 04318 Leipzig, Germany;* [7]*Universität Leipzig, Leipziger Institut für Meteorologie, Stephanstr. 3, 04103 Leipzig, Germany*

(Manuscript received 20 December 2010; in final form 5 May 2011)

ABSTRACT

Ground-based high spectral resolution measurements of downwelling radiances from 800 to 1200 cm^{-1} were conducted between 20 January and 6 February 2008 within the scope of the SAMUM-2 field experiment. We infer the spectral signature of mixed biomass burning/mineral dust aerosols at the surface from these measurements and at top of the atmosphere from IASI observations. In a case study for a day characterized by the presence of high loads of both dust and biomass we attempt a closure with radiative transfer simulations assuming spherical particles. A detailed sensitivity analysis is performed to investigate the effect of uncertainties in the measurements ingested into the simulation on the simulated radiances. Distinct deviations between modelled and observed radiances are limited to a spectral region characterized by resonance bands in the refractive index. A comparison with results obtained during recent laboratory studies and field experiments reveals, that the deviations could be caused by the aerosol particles' non-sphericity, although an unequivocal discrimination from measurement uncertainties is not possible. Based on radiative transfer simulations we estimate the aerosol's direct radiative effect in the atmospheric window region to be 8 W m^{-2} at the surface and 1 W m^{-2} at top of the atmosphere.

1. Introduction

It is well known that mineral dust aerosol in the Earth atmosphere significantly influences weather and climate in several ways, which are summarized in Ansmann et al. (2011) and references therein. In the publication at hand we focus on the characterization of the aerosol's interaction with electromagnetic radiation in the thermal infrared (TIR) atmospheric window region between 800 and 1200 cm^{-1} (8.3–12.5 μm). The aerosol radiative properties in this spectral region are important since they govern the amount of thermal energy transmitted through the atmosphere into space and thus affect the local and global radiation budget. As a consequence weather and climate models rely on an adequate representation of the aerosol radiative properties in order to account for radiation-induced processes. Furthermore several remote sensing instruments (e.g. IASI and AIRS) infer physical quantities such as sea surface temperature (SST) or ozone concentration from radiation measurements in the atmospheric window. The accuracy of the retrieval is deteriorated in the presence of aerosols within the instrument's field of view if the underlying radiative transfer model (RTM) describes the radiative properties in an inappropriate way (Sokolik, 2002).

From a theoretical point of view the scattering problem would seem simple at first glance: given a plane electromagnetic wave scattered by an arbitrarily shaped particle in air with known refractive index (or equivalently dielectric function), the Maxwell equations guarantee a unique solution for the electromagnetic

*Corresponding author.
e-mail: claas.koehler@dlr.de
DOI: 10.1111/j.1600-0889.2011.00563.x

radiation field. In practice, however, it turns out that analytical solutions to the Maxwell equations are only available for a very limited range of highly symmetric geometries such as spheres or infinite cylinders, while numerical methods allowing for a wider range of shapes are usually restricted to a certain domain of size parameters (i.e. ratio of characteristic geometric length to wavelength). An excellent overview over contemporary approaches to the scattering problem is given by Nousiainen (2009) while an in-depth analysis is provided by Rother (2009).

The simple geometries for which numerical solutions are available are contrasted by the complex microphysical composition of real aerosol-forming matter, which is often irregular in shape and may consist of agglomerates of different materials with inclusions or coatings. In order to predict the radiative behaviour of these particles two assumptions are commonly made: the complex shape is replaced by a more symmetric one (e.g. sphere) and the inhomogeneous mixture of mineral components is replaced by a homogeneous medium with one effective refractive index. The errors introduced by the above-mentioned approximations however are not sufficiently characterized and no widely accepted procedure for modelling the radiative properties of atmospheric mineral dust aerosol has evolved so far.

Although Hoidale and Blanco (1969) report TIR measurements of dust aerosol and identify a distinct spectral signature, the TIR radiative properties of mineral dust have long been neglected compared to the UV/VIS.

Sokolik et al. (1998) perform simulation studies to assess the radiative forcing of mineral dust aerosols in the TIR atmospheric window region and note the sensitivity of their simulations towards the assumed refractive index of the aerosols. They also conclude, that since the mineral composition of dust is likely to vary with source region, it would be advantageous to calculate the bulk refractive index from the refractive indices of its mineral constituents rather than specifying one refractive index for dust. Highwood et al. (2003) present airborne high spectral resolution measurements over a dust layer and confirm the theoretical predictions of a distinct spectral signature. They further conclude, that ground-based measurements of the downwelling radiation should be superior to their measurements of upwelling radiation, as the latter suffer from uncertainties in surface emissivity and temperature. A detailed simulation study by Hollweg et al. (2006) analysing the combined error budget of radiative transfer (RT) simulations and Fourier transform infrared (FTIR) measurements gives further indication that aerosol optical depth (AOD) as commonly encountered in the vicinity of source regions should be detectable with state-of-the-art instrumentation and RT modelling. These findings motivated us to measure downwelling radiances during the SAMUM-2 campaign, in order to attempt a column closure for downwelling radiances in the atmospheric window region.

A number of field experiments dedicated at least partly to mineral dust aerosol have been conducted within the last decade. In the following paragraphs we give an overview over the most important findings of these experiments along with selected results from related modelling studies.

Hansell et al. (2008) analyse ground-based measurements of downwelling radiation recorded in 2004 with the AERI instrument during the UAE^2 campaign close to Abu Dhabi, United Arab Emirates. They present a method to retrieve dust AOD from the AERI measurements based on brightness temperature differences (BTD) between different AERI channels by choosing from a set of pre-calculated BTDs the one which most closely resembles the observed BTDs. For the retrieval, dust is modelled using the refractive index model of Volz (1973). In a later paper (Hansell et al., 2010) the AOD retrieval described earlier is applied to AERI spectra measured during the 2006 NAMMA campaign, which was conducted on the island of Sal, Cape Verde, in parallel to the AMMA study.

Turner (2008) retrieves dust composition and size distribution from AERI measurements obtained during the 2006 AMMA campaign in Niamey, Niger, assuming spherical particles consisting of a three-component external mixture of Kaolinite, Quartz and Gypsum. It is concluded from the observations that Kaolinite and Gypsum are the most abundant minerals while Quartz seems to play a minor role. The retrieval is based on an optimal estimation strategy using microwindows distributed over the spectral region from 770 to 1200 cm^{-1} excluding the interval 980–1080 cm^{-1}, where a strong ozone absorption band disturbs the retrieval, as the author states.

Bharmal et al. (2009) utilize the 2006 AERI data from Niamey for forcing calculations along with satellite observations and Thomas and Gautier (2009) perform TIR absorption measurements during the same period of time at M'Bour, Senegal, within the scope of the AMMA campaign. They report a TIR direct radiative effect (DRE) at bottom of the atmosphere (BOA) of 2–10 Wm^{-2} and 2–11 Wm^{-2} at top of the atmosphere (TOA). Furthermore, the measurements of Thomas and Gautier (2009) display a spectral shift of approximately 40 cm^{-1} towards lower frequencies when compared to simulations assuming spherical model particles and several different refractive index models including both internal and external mixtures. The effect is most prominent in the spectral interval 1000–1100 cm^{-1} and according to the authors it is caused by the approximation of non-spherical particles with spherical ones.

Although many of the aforementioned measurements characterize the aerosol DRE and perform several sensitivity studies on their input parameters, we are currently not aware of any study which performs a radiative column closure taking into account vertically resolved measurements of both size-distribution and particle composition to model TIR radiances at BOA and TOA.

In this paper we present the results obtained from ground-based FTIR measurements in the atmospheric window region from 800 to 1200 cm^{-1} (8–12 μm) during the SAMUM-2 field campaign conducted from 20 January to 6 February 2008 at Praia on the island of San Tiago, Cape Verde. Our measurements show

a distinct spectral signature attributable to mineral dust which we compare in a case study to RT simulations assuming spherical particles ingesting observations of other SAMUM-2 groups. We complete our analysis with upwelling radiances at TOA from satellite-based FTIR measurements and calculate the aerosol DRE by means of RT simulations.

2. Experimental approach & instrument description

Downwelling TIR radiances were measured using a Model 102 FTIR spectrometer manufactured by Design and Prototypes (D&P). The instrument is originally designed for field measurements of minerals and rocks. Its key features are a spectrometer core consisting of two laterally moving prisms and a sandwich-type MCT/InSb detector spanning a spectral range from 650 to 3000 cm^{-1} (MCT: 650–1800 cm^{-1}, InSb: 1800–3000 cm^{-1}). A detailed description of the prototype has been published by Korb et al. (1996). The Model 102 has a very compact design and its portability allows for simple and cost-effective transport and make the instrument easy to use in the field. A rotatable mirror enables measurements at arbitrary zenith angles. One of the main disadvantages is the operating procedure of the instrument, which requires an operator to be present during measurements and is thus not suited for automated recording of long time series. On the other hand an operator can interactively select scene and time of observation for each measurement, which makes, for example, automatic cloud screening superfluous.

The Model 102 was operated from 20 January to 6 February 2008 at the SAMUM-2 measurement site at Praia Airport (14.95°N, 23.48°W) on the Island of San Tiago, Cape Verde, along with the other ground-based instrumentation described in detail in Ansmann et al. (2011). Due to the manual measurement procedure, data acquisition was conducted mostly during daytime at several zenith angles. The results presented within this paper however were all recorded at a zenith angle of zero degrees. Upwelling radiances shown throughout this study are taken from the IASI Level 1c product available via the EUMETSAT Data Centre (https://archive.eumetsat.int/umarf/). A summary of selected instrument core quantities for IASI and the D&P Model 102 FTIR is supplied in Table 1.

Table 1. Core data of the instruments used in this study: The D&P Model 102 portable FTIR for ground-based measurements and the IASI FTIR on-board METOP-A

	D&P Model 102	IASI
Spectral Range (cm^{-1})	700–3000	650–2750
Resolution (cm^{-1})	6	0.35–0.5
NEΔT (K)	0.2	0.1–0.5

In the following sections we describe the calibration and validation procedure for the ground-based FTIR instrument and discuss the effects of a bias most likely caused by detector non-linearity.

2.1. Calibration

As we aim to employ the Model 102 for measurements of downwelling atmospheric TIR radiances, calibration is a challenging issue, because the spectral variation of atmospheric radiances is much larger than radiances typically emitted by solid surfaces, such as soil or mineral samples at ambient temperature. Usually the detector response is assumed to depend linearly on the incoming radiation at a given wavenumber with a constant offset caused by background radiation within the instrument. In this case response and offset can be determined from two blackbody measurements at different temperatures, where the temperatures are chosen, such that the intensities of the emitted radiation bound the expected interval of measured intensities on the high and low side. However this method is not feasible for atmospheric radiance measurements, since observed brightness temperatures may be as low as 220 K. Operating a blackbody at this temperature is a challenging task in a laboratory but almost impossible in the field as ambient humidity causes the formation of ice. Thus it is a common procedure to use blackbody measurements at higher temperatures and extrapolate the detector response to lower temperatures/intensities. This procedure may yield erroneous results, if the detector displays non-linear behaviour, especially if the intensities of the incoming radiation lie significantly outside the interval of calibration. This issue is well known and several methods have been suggested to correct for it depending on the instrument (e.g. Knuteson et al., 2004b; Fiedler et al., 2005; Kleinert et al., 2007). However all of these methods require in essence the interferogram of an individual non-linear detector. This makes them unsuitable for the Model 102, since the interferograms for both detectors—the MCT and the InSb—are added by the analog electronics. This becomes an issue as non-linearity causes the MCT to create out-of-band signal components overlapping with the InSb in-band frequencies. Thus these signals become virtually inseparable, preventing a correction of the effect. As a consequence we have to limit ourselves to a characterization of the associated bias.

Our calibration procedure involves a bandpass filter to remove electronic noise from the interferograms to improve the following detection of the point of zero path difference (ZPD) of each interferogram. Since the spectrometer is made of potassium bromide, dispersion causes the ZPDs of MCT and InSb to differ and to depend on the spectral distribution of the incoming radiation. In order to compensate for the ZPD shift between blackbody and ambient spectra, we detect the ZPD for a part of the spectrum dominated by water absorption, which is very similar for atmospheric and blackbody measurements. A detailed description of this method can be found in Koehler et al. (2009).

After the ZPD correction we co-add 50 measurements in each scan direction of the FTIR mirror, transform the interferograms into spectra by Fast Fourier Transformation and calibrate as suggested by Revercomb et al. (1988). For this calibration we use the spectra of three blackbodies at different temperatures and determine the instrument response and offset using a linear least-squares fit. This is similar to the procedure described in Lindermeir et al. (1992) but with constant blackbody temperatures. After calibration we average the real part of both scanning directions to obtain the measured spectrum.

The calibration measurements are obtained with the temperature adjustable blackbody delivered with the instrument mounted to the instrument fore-optics. This modus operandi ensures that all optical components including the rotatable mirror are calibrated and consequently takes into account all effects linear in radiance (e.g. detector response, internal emission, absorption by atmospheric gases within the instrument and absorption by optical components). The emissivity of the blackbody is specified by the manufacturer to be greater than 0.994 and a comparison with measurements of the high-precision blackbody described in Fiedler et al. (2005) gave no indication of a lower value. The temperature stability of the blackbody is checked with an internal PT100 thermistor and is usually less than 0.1 K. The set-temperatures used for calibration are 3 °C, 13 °C and 23 °C and are commonly reached within less than 60 s, which is again checked using the built-in thermistor. A calibration as described earlier is performed roughly every 45 min and takes approximately 15 min. We ensure that the calibration remains constant in time by comparing two sets of blackbody measurements acquired before and after the measurement, respectively. The calibration is only accepted, if both calibrations agree within measurement tolerance.

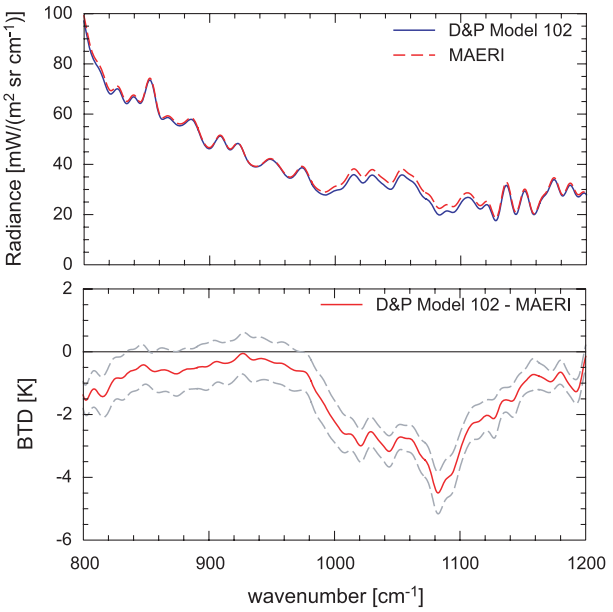

Fig. 1. Results from coincident colocated zenith measurements of the D&P Model 102 and MAERI obtained on 14 May 2009 at Miami during cloud-free conditions. The MAERI integration time is 120 s centred at 2055 UT, while the Model 102 spectra were integrated over a time span of 180 s centred at 2053 UT. Spectra are convolved to a resolution of 10 cm^{-1}. The top panel displays measured radiances and the bottom panel displays the residual BTD. The light grey lines in the residual plot indicate the statistical standard deviation over all averaged measurements of the D&P Model 102.

2.2. *Validation*

Although several methods of instrument validation are possible, measurements of well-characterized blackbodies at different temperatures under laboratory conditions are usually the method of choice. We cooperated with the UK MetOffice and undertook measurements similar to those described by Fiedler et al. (2005) to correct non-linearity effects in the ARIES spectrometer by means of a series of low-temperature blackbody measurements down to 210 K. Unfortunately the Model 102 performed quite poorly, since the addition of interferograms from each detector makes it difficult to obtain a reliable ZPD detection. As the procedure for atmospheric spectra outlined in Koehler et al. (2009) is based on water absorption bands, it is not applicable due to the fact that instrument and blackbody were purged with nitrogen to avoid ice formation. Thus no water absorption bands usable for correction are present in the spectra. Furthermore it became obvious, that the high amount of background radiation emitted by the spectrometer obfuscates the low intensity radiation emitted by the blackbody and that the out-of-band signal originating from the MCT non-linearity creates large artefacts in the InSb spectral domain at low intensities, rendering the InSb useless for atmospheric observations.

Nonetheless we figured, that atmospheric measurements were capable of producing sensible results in the MCT domain, since we had achieved quite promising agreements between RT simulations and atmospheric measurements before. However we refrained from validating our measurements with RT simulations, since they were intended to be compared to the latter for evaluation purposes. Thus we decided to validate our measurements with coincident measurements of the MAERI (Minnett et al., 2001) obtained during an instrument comparison workshop at the Rosenstiel School of Marine and Atmospheric Sciences of the University of Miami organized by the Committee on Earth Observation Satellites (CEOS). The MAERI is an FTIR based on the AERI (Knuteson et al., 2004a), which is specifically designed for measurements of TIR radiation emitted by the atmosphere and which is well validated (Knuteson et al., 2004b). Figure 1 shows a comparison of two coincident measurements under clear-sky conditions in the TIR atmospheric window domain. The integration time of the MAERI spectrum is 120 s while two consecutive measurements of the Model 102 were averaged totalling 180 s of integration time. Both spectra were apodized

with a triangle function to coarsen the resolution to 10 cm^{-1} in order to compensate for the higher resolution of the MAERI. It can be observed that both measurements agree within the statistical error for wavenumbers smaller than 1000 cm^{-1}, while a bias of up to 4 K is apparent for larger wavenumbers. This bias is most likely attributable to MCT detector non-linearity and appeared to be constant over all measurements taken within the scope of the comparison. However, it should be noted, that the influence of detector non-linearity is to some extent scene dependent, since it scales with the radiative flux incident on the detector. Due to the fact, that the amount of precipitable water was relatively high (33 mm measured by a radiosonde launched at Miami Airport at 2306 *UT*), the effect may be more pronounced under drier conditions or at lower temperatures leading to lower amounts of downwelling radiation. Unfortunately this is the only benchmark comparison available to us and we cannot provide a more reliable estimate of the measurement uncertainty associated with detector non-linearity.

3. RT Simulations

The interpretation of column-integrated spectral radiance measurements requires comparison to simulated radiances, since the multitude of gas absorption lines and scattering particles interact with radiation in a non-trivial way and their individual contribution to the measured spectrum cannot be separated without the help of an RTM. Several RTMs such as LibRadTran (Mayer and Kylling, 2005) or LBLRTM (Clough et al., 2005) are available for download, but we are currently not aware of any model which takes advantage of object oriented programming and allows for effective parallelization on modern multiprocessor architectures. We developed a new code called PIRATES (*P*rogrammer's *I*nterface to *Ra*diative *T*ransf*e*r Algorithm*s*), which will be described in the following sections along with its input parameters. In addition, we provide comparisons with AERI observations and LBLRTM calculations created within the framework of the CIRC comparison (Oreopoulos and Mlawer, 2010).

3.1. The PIRATES model

PIRATES is a library written in C++ which implements solutions for common problems in RT, such as line-by-line gas absorption calculation, numerical solution of the RT equation, or calculation of single scattering properties of particles. A key feature of PIRATES is the ability to take advantage of multicore architectures, which have become standard on modern PCs, by running several threads in parallel, thus achieving a significant speedup of the simulations.

The model calculates the optical depth of absorbing gases line-by-line with input parameters from the latest version of the HITRAN database (Rothman et al., 2009) assuming a Voigt line profile. In order to speed up the line-by-line calculations the interpolation method proposed by Kuntz and Hoepfner (1999) has been implemented into the model. Furthermore a band averaging algorithm may be chosen, which significantly accelerates the solution of the RT equation. The algorithm uses a Gauss–Legendre quadrature rule to average the total transmittance from the sensor to every layer over equal-spaced spectral intervals with user-specifiable width.

In addition to the line-by-line optical depth we implemented the latest version 2.5 of the MTCKD continuum described in Clough et al. (2005). Furthermore we use parameterized cross sections included in the HITRAN distribution for those species for which no line-by-line information is available, most notably CCl4, CFC-11, CFC-12 and HCFC-22, which all have a significant contribution in the spectral domain 800–1200 cm^{-1}.

The calculation of optical depth, single scattering albedo and scattering phase function for spherical particles is performed using the algorithms described in Wiscombe (1980). Although a FORTRAN version of these algorithms is available online, the code was ported to C++ to allow for thread-safe execution in shared memory applications, which allow to significantly speed up the calculations on multicore machines. Since the application of Mie theory for the calculation of non-spherical particles is known to be insufficient in many cases (Nousiainen, 2009), PIRATES includes a database for non-spherical particles, which in turn interfaces to the scattering database of Schmidt et al. (2009) and Otto et al. (2009).

In order to model the refractive index of the observed aerosols we compiled a database from literature called DIRAC (*D*atabase for the *I*ndex of *R*efraction of *A*erosol *C*omponents) which is directly accessible from PIRATES enabling simple generation of bulk aerosol refractive indices from the optical constants of the individual mineral aerosol constituents. The data sets used for this study are listed in Table 2. Note that the data for Orthoclase may contain typographical errors, since it was not possible to reproduce the published plots with the oscillator parameters given in the same publication. It was included anyway, because we could not find more reliable data in published literature. Furthermore no published optical constants for sodium sulphate are available to the best of our knowledge, which is why we represent sodium sulphate by a mixture of ammonium sulphate and gypsum, because the refractive indices between 800 and 1200 cm^{-1} are dominated by the ν_3 absorption band of the sulphate anion. It is however not clear, how good this approximation is and might be a possible source of error.

The RT equation is solved in the plane parallel approximation using the discrete ordinate method by calling the DISORT code as described by Stamnes et al. (1988). Again some of the DISORT routines had to be ported to C++ in order to allow for thread-safe execution of the program in shared memory applications.

In order to validate the model we chose to compare it to LBLRTM and to AERI observations. To make sure that the cases selected for comparison have been checked independently and

Table 2. References for the refractive index data used to calculate bulk aerosol optical constants

Mineral species	Reference
Albite	Mutschke et al. (1998)
Ammonium sulphate	Toon et al. (1976)
Anorthite	Aronson and Strong (1975)
Calcite	Querry et al. (1978)
Chlorite	Mooney and Knacke (1985)
Gypsum	Long et al. (1993)
Hematite	Glotch et al. (2006)[a]
Illite	Glotch et al. (2007)
Kaolinite	Glotch et al. (2007)
Montmorillonite	Glotch et al. (2007)
Sea salt	Shettle and Fenn (1979)
Orthoclase	Aronson (1986)[a,b]
Quarz	Henning and Mutschke (1997)
Soot	Sutherland and Khanna (1991)

[a] Averaged over principal axes of dielectric tensor.
[b] Data probably contain typographical errors, but no other data available.

to minimize the chance of errors we used PIRATES to calculate the clear-sky cases one to four of the CIRC comparison (Oreopoulos and Mlawer, 2010) available at http://circ.gsfc.nasa.gov. We compare downwelling irradiances with LBLRTM calculations provided by CIRC and furthermore accessed the online archive of the Atmospheric Radiation Measurement (ARM) website (http://www.arm.gov) provided by the U.S. Department of Energy to retrieve the AERI spectra for each CIRC case. The comparison of PIRATES spectra with LBLRTM irradiances (left-hand column) and AERI-measured radiances (right-hand column) is shown in Fig. 2.

Cases 1–3 stem from the Southern Great Plains (SGP) ARM site and represent scenarios of low (12 mm PWV), high (49 mm PWV) and moderate (23 mm PWV) amounts of precipitable water vapour, respectively. Case 4 is based upon observations of a very cold and dry (3 mm PWV) atmosphere at the Northern Slope of Alaska (NSA) ARM site.

Simulated and measured radiances plotted in Fig. 2 (right-hand column) agree within 5 mW m^{-2} sr^{-1}, which is comparable to the residuals usually obtained with LBLRTM. Integration of the residuals reveals a small underestimation of the simulated downwelling radiance by an average of 0.6, 0.4, 1.3 and 1.2 mW m^{-2} sr^{-1}, respectively, for the cases 1–4. A possible explanation for this is a known warm bias of approximately equal magnitude, apparently common among the AERI instruments (Turner, 2008).

Regarding the irradiances in Fig. 2 (left-hand column), no systematic bias compared to LBLRTM is observable and calculation of the fluxes reveals deviations of 0.7, −0.6, −0.4 and 0.9 W m^{-2}, respectively, for the cases 1–4.

3.2. Model input

In order to simulate the atmospheric conditions observed during the measurements we use vertical profiles of temperature, pressure and relative humidity obtained from radiosondes launched at the measurement site. These profiles usually extend up to a height of 15–20 km and are further extended to 100 km by appending profiles from the MIPAS tropical-daytime atmosphere compiled by J. Remedios (available at http://www.atm.ox.ac.uk/RFM/atm). The temperature and relative humidity data sets are smoothed and reduced in vertical resolution to avoid excessive computation time. Furthermore we scale the carbon dioxide profile by a constant factor to obtain a total column mixing ratio of 380 ppm and similarly scale the ozone profile such that the total column density agrees with data inferred from the GOME-2 instrument (Loyola et al., 2011) on-board METOP-A.

The aerosols are modelled by a variable number of layers at altitudes matching LIDAR observations coincident with our measurements (Tesche et al., 2011; Groβ et al., 2011). Within each layer we assume the particle number concentration to be representable by a 4-modal log-normal distribution of the form

$$\frac{\mathrm{d}N(r)}{\mathrm{d}r} = \sum_{i=1}^{4} \frac{N_i}{r\sigma_i\sqrt{\pi}} \exp\left[-\frac{\left(\ln\frac{r}{r_i}\right)^2}{\sigma_i^2}\right], \tag{1}$$

with volume equivalent radius, $r = D_p/2$, mean radius $r_i = 1/2$ $\mathrm{CMD_i}$ and standard deviation

$$\sigma_i = \sqrt{2}\ln \mathrm{GSD}_i. \tag{2}$$

N_i, $\mathrm{CMD_i}$ and $\mathrm{GSD_i}$ are the particle number concentration, count median diameter and geometric standard deviation of each mode, respectively, as provided in Weinzierl et al. (2011). In accordance with Lieke et al. (2011) we split each size distribution into three intervals

$$\begin{aligned} I_1 &= \{r \mid 0\,\mu\mathrm{m} < r \leq 0.25\,\mu\mathrm{m}\};\\ I_2 &= \{r \mid 0.25\,\mu\mathrm{m} < r \leq 1.25\,\mu\mathrm{m}\};\\ I_3 &= \{r \mid r > 1.25\,\mu\mathrm{m}\}; \end{aligned} \tag{3}$$

assigning one refractive index per interval. The bulk refractive index for each layer and interval is obtained from the individual refractive indices listed in Table 2 using a simple volumetric mixing rule, where the weights are chosen to match the single particle analysis obtained from ground-based (Kandler et al., 2011a) and airborne (Lieke et al., 2011) measurements. Since the end-members of several silicate mineral groups are analytically hard to separate (Kandler et al., 2011b), we had to choose them in a physically reasonable manner within the uncertainty of the measurements reported by Kandler et al. (2011a) and Lieke et al. (2011) yielding a possible source of error.

In order to appropriately model the boundary conditions we make different assumptions for the simulation of the upwelling and downwelling radiation: Since the influence of surface emissivity and surface temperature on the upwelling radiance at TOA

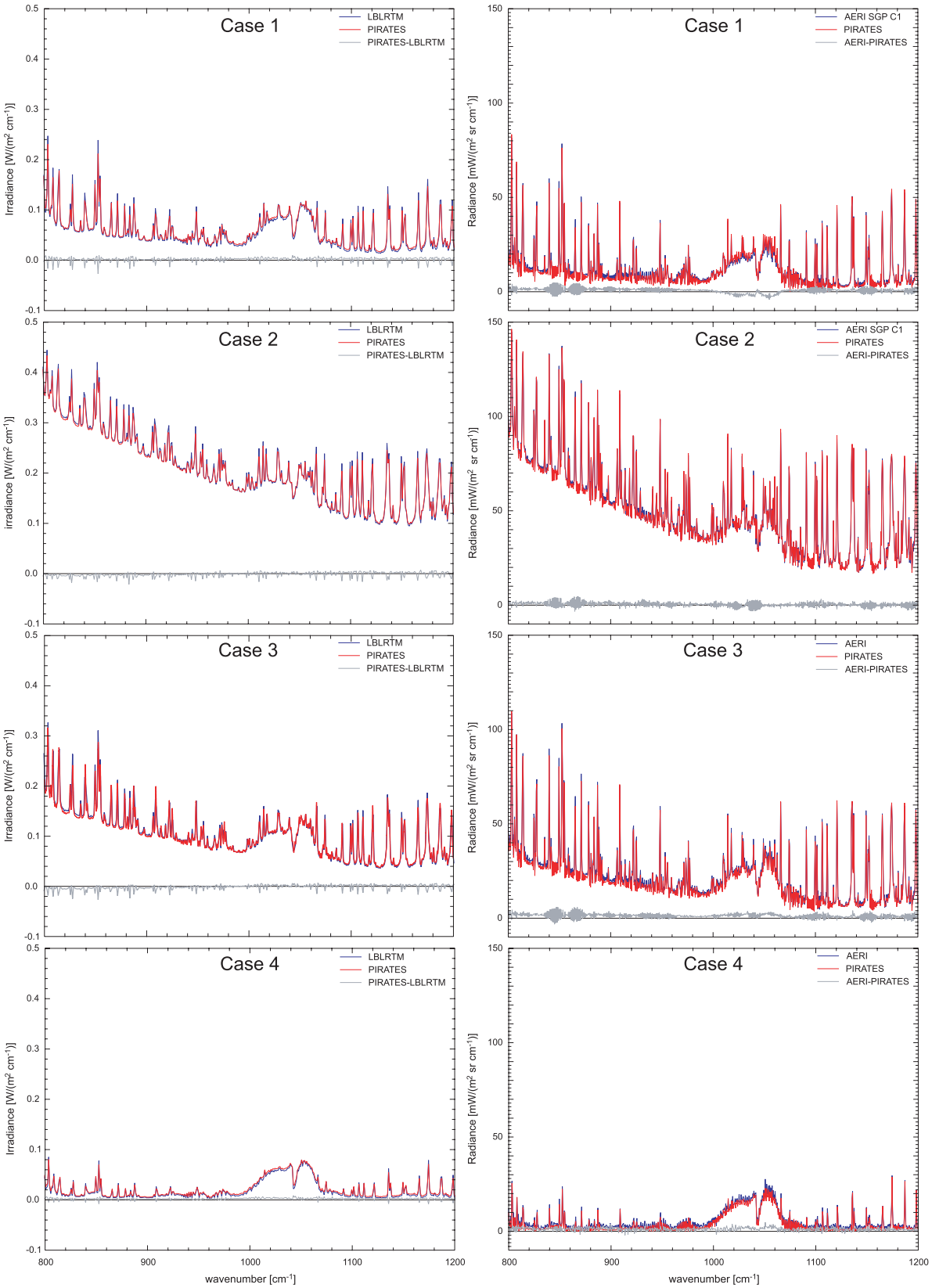

Fig. 2. Intercomparison of PIRATES simulations with LBLRTM irradiances (left-hand column) and measured AERI radiances (right-hand column).

is very strong we restrict the satellite observations to cases, where the entire field of view is covered by water and assign the SST provided in the METOP-A combined sounding product. It must be taken into account, however, that the thus obtained SST could be biased by the presence of the aerosols subject to this study, depending on the retrieval algorithms used. The sea surface emissivity is calculated from Fresnel's equation with the refractive indices provided in Bertie and Lan (1996), which are corrected for salinity as suggested in Friedman (1969).

Since the downwelling radiation measurement at BOA was conducted at Praia airport less than 1 km off the coast, we expect an influence of both land and sea surface. While the sea surface emissivity can be readily calculated as described earlier, the modelling of a land surface dominated by particulate matter is far more complicated. On the other hand it only contributes to the measured radiance via radiation scattered back into the instrument, which is expected to be far less influential than the direct emission observed at TOA. Emissivity measurements with the Model 102 indicate an emissivity of $\epsilon = 0.9 \pm 0.1$ with very little spectral variation over the TIR atmospheric window region. Thus we assume this value throughout our simulations and assign a ground surface temperature measured by a PT100 thermistor at a sandy spot close to the measurement site. While the surface is assumed to be representative for the island surface it has to be stated, that surface temperature measurements show large diurnal variations (290–320 K depending on incoming solar radiation and surface material). The resulting uncertainties are discussed in Section 4.3.

4. Results

As mentioned earlier our goal is to isolate the aerosol radiative effect based on measurements performed at BOA and TOA. In order to do so we have to eliminate the effect caused by gas absorption/emission, which is achieved by subtracting a simulated spectrum for a clear-sky atmosphere from the measured spectrum. While the quantities and parameters ingested into the simulations are mostly obtained from measurements, some assumptions are required too, as described in detail in Section 3.2. Thus we will first discuss the effect of several associated uncertainties on the simulated clear-sky spectra in Section 4.1. We will then proceed to present the results of our measurements in Section 4.2 by providing an overview over the spectral signatures of mineral dust and biomass-burning aerosol as observed during the SAMUM-2 campaign. We conclude with results from a case study examining the radiative impact of the observed aerosol based on RT simulations in Section 4.3.

4.1. *Sensitivity of selected quantities towards input parameters*

The spectral region from 800 to 1200 cm^{-1}—also called 'atmospheric window'—is often used for infrared observations since it is considerably less affected by gas absorption and emission than most other parts of the TIR spectral domain. Nevertheless, water vapour and ozone notably influence atmospheric radiation in the atmospheric window and several weak absorption bands caused by a variety of trace gases have to be taken into account too. Since Hollweg et al. (2006) provide an exhaustive analysis of uncertainties affecting the accuracy of RT simulations covering this spectral region, we limit ourselves to an analysis of the quantities most relevant for this study, that is, the vertical profiles of water vapour, ozone and temperature.

The procedure we will follow is similar in all three cases: We start with a tropical standard atmosphere as reference and successively alter the profiles of interest in a way assumed representative for measurement uncertainties (or errors in our assumptions, where no measurements are available). Thereby we will use the BTD spectra obtained by subtracting a simulated BT spectrum for the manipulated atmosphere from the simulated BT spectrum for the reference atmosphere. We choose a relatively coarse resolution of 10 cm^{-1}, since aerosols are expected to have a rather smooth spectral signature as compared to the numerous gas absorption lines, which might obfuscate the aerosol features at a higher resolution. Although the sensitivity studies presented here are exclusively clear-sky spectra (i.e. without aerosols), we chose the same resolution to allow for a simpler comparison to the results shown in the following sections.

As stated earlier we use temperature profiles measured by radiosondes, which usually extend to an altitude between 15 and 25 km. Deviations of measured and exact profile may, for example, occur due to measurement uncertainties, drift of the radiosonde from the measurement location or by temporal variations of the temperature profile due to meteorological processes. We constrain these errors to three simple cases: First we shift the original temperature profile by 1 K and 5 K, respectively, to give a general feeling how temperature changes propagate to the output spectrum. In addition, we simulate a heating effect at the surface by assuming an altitude dependent increase $\Delta T(z)$ in air temperature defined by

$$\Delta T(z) = \begin{cases} 0\,\mathrm{K}, & z > 1.5\,\mathrm{km} \\ \dfrac{10}{3}\dfrac{\mathrm{K}}{\mathrm{km}}(1.5\,\mathrm{km} - z), & 1.5\,\mathrm{km} < z \leq 0\,\mathrm{km}. \end{cases} \quad (4)$$

The original and manipulated temperature profiles for this case are displayed in Fig. 3d. Furthermore we have to make assumptions on the temperature profile above the tropopause, where no measurements are available. Here we examine the consequences of exchanging the temperature profile of a tropical atmosphere with the MIPAS tropical day atmospheric temperature profile. Both, the original and the modified profile, are plotted in Fig. 3c. The resulting BTD spectra for each of the four cases described earlier are shown in Fig. 4c for a downlooking sensor at TOA and in Fig. 4f for an uplooking sensor at BOA. As was to be expected, the overall increase of 5 K applied to the whole profile is a worst case scenario at both BOA and TOA, while the

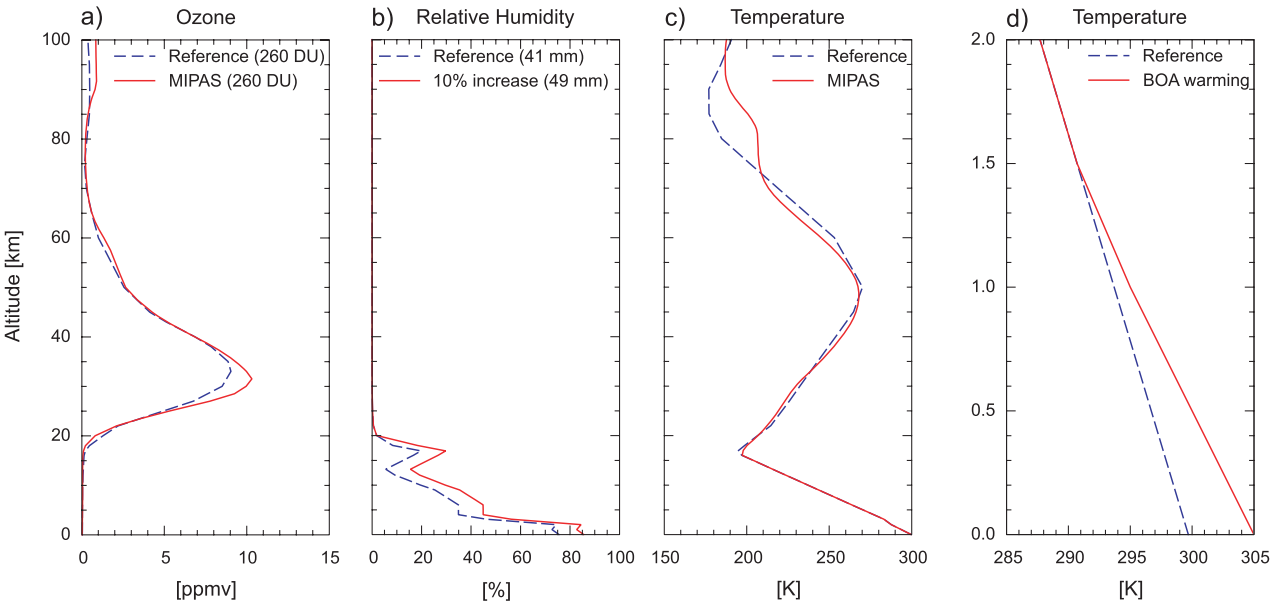

Fig. 3. Profiles of ozone, relative humidity and temperature used in the sensitivity studies. Numbers in brackets indicate total column of ozone (a) and precipitable water (b). Note the different altitude scale in (d).

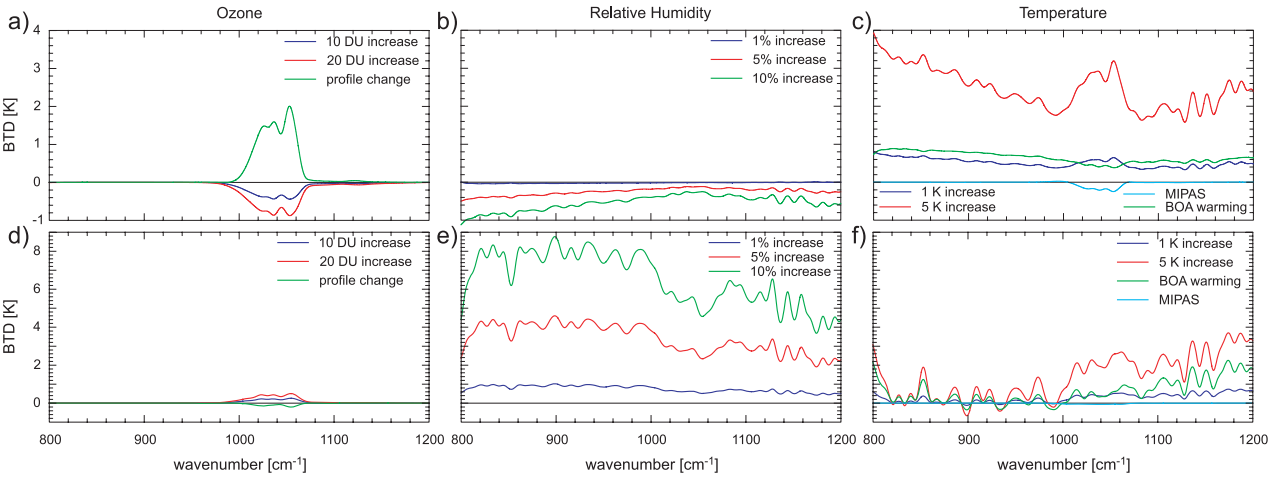

Fig. 4. Simulated BTD resulting from subtraction of spectra obtained under the assumption of a modified profile from the reference tropical standard atmosphere. Figures a–c (top row) display the effect on the upwelling radiation at TOA while Figures d– f visualise the sensitivity of the downwelling radiation at BOA. Note that different BTD scales are used for BOA and TOA spectra.

exchange of the profiles above the tropopause shows the least differences. Furthermore the plots indicate, that a ground based sensor is quite sensitive to temperature changes in the lower troposphere.

Since no ozonesondes were launched within the scope of the SAMUM-2 field experiment we have to rely on satellite retrieved data for ozone column densities, which we incorporate by scaling the ozone volume mixing with an altitude-independent factor to fit the measured column density. Possible sources of error arising from this concept are uncertainties in the retrieval (possibly caused by the presence of aerosol layers) and changes in the ozone profile from our assumed profile, since no additional profile information is used. We account for such errors by first investigating the effect of increasing the total ozone column density by 10 and 20 Dobson units (DU), respectively, with 10 DU being a typical value for local variations. Furthermore we examine the effect of profile variations by exchange of the ozone profile with the ozone profile of the MIPAS tropical day atmosphere, the latter being scaled to the same ozone column density as the default atmosphere (260 DU). The MIPAS profile is plotted in Fig. 3a together with the default profile. The resulting BTD spectra for the mentioned cases are provided in Fig. 4a (TOA) and Fig. 4d (BOA). While an observer at BOA notes only minor effects due to the variations, the change caused

in the TOA spectra is remarkable, especially for the exchange of the vertical profile.

Finally we would like to assess the consequences of uncertainties in the atmospheric water vapour concentration. Again the profile included in our simulations is obtained from radiosonde measurements. This profile may be inaccurate due to measurement uncertainties or due to diurnal atmospheric variations. The radiosondes used throughout the campaign were Vaisala RS92-SGP and RS80. It has been shown by Vömel et al. (2007) that both sonde types are susceptible to a considerable dry bias during daytime measurements, which is caused by solar heating of the humidity sensor. An empirical correction for this bias has been suggested by Cady-Pereira et al. (2008), which is derived from soundings performed at the ARM SGP site between 1998 and 2005. However, Vaisala improved the humidity sensor of the RS92 for sondes sold after 2006 and all RS92 sondes launched within the scope of SAMUM-2 were equipped with this improved sensor type. Due to this hardware change and a series of tests with the correction algorithm of Cady-Pereira et al. (2008) which showed no obvious improvements of the data, we chose not to correct the RS92 measurements. Furthermore we could not detect systematic inconsistencies between the RS92 and RS80 measurements, which might be explained by the fact, that the RS80 were usually launched at night, when no radiation dry bias occurs. Thus we did not apply any correction to the RS80 measurements either. It should be noted, however, that Vaisala introduced an improved humidity retrieval algorithm into their evaluation software in December 2010, which seems to cause a systematic height-dependent increase in humidity judging from plots published on their website. Since we currently do not have access to this software, we cannot evaluate the effect this might have on our results, but we would like to mention it as an additional source of uncertainty.

Since the occurrence of a significant amount of water vapour is limited to the (lower) troposphere, we do not investigate uncertainties due to extension of the measured radiosonde data to TOA. Instead we determine the consequences of vertically constant increases in the relative humidity below 20 km of 1%, 5% and 10%. Figure 3b is a plot of the default relative humidity (dashed) and the 10% increased profile. Again the changes in BTD at BOA and TOA are displayed in Figs 4b and e. It is obvious from these plots, that a BOA-based sensor is far more sensitive to the described variations in relative humidity compared to an instrument looking down from TOA. In addition, we would like to stress that the (simulated) water vapour absorption is almost exclusively caused by continuum effects and not by individual absorption lines in the atmospheric window. While the line parameters included in the HITRAN database are inferred from laboratory studies, the continua are based on a semiempirical model, the parameters of which depend predominantly on spectral atmospheric measurements. As Hollweg et al. (2006) rightfully point out, the extent to which biases in these measurements (e.g. due to an incorrectly modelled atmospheric state caused by the presence of aerosols) affect the continua is not clear and could introduce a non-negligible source of error.

As a consequence of these sensitivity studies we will limit our survey to BOA measurements which were acquired temporally close (i.e. less than 1 h prior or post) to radiosonde measurements, since the results indicate that diurnal changes in temperature and relative humidity may cause significant variations in the downwelling radiation. Furthermore we would like to emphasize the impact of ozone profile changes at constant integrated column densities which amount to an uncertainty in brightness temperature of almost 2 K between 1020 and 1060 cm^{-1}, since no instruments capable of measuring this quantity were present during SAMUM-2. As a conclusion it must be stated that the potential to extract aerosol effects from TOA spectra in this spectral region is quite limited within the scope of this study. Furthermore we would like to add, that the ozone column densities taken from the IASI combined sounding product seemingly exceed the GOME-2 values by approximately 10–20 DU for all cases investigated in the course of our SAMUM-2 data analysis. While the number is too small for a reliable statistic, it might nonetheless indicate an aerosol induced bias in one (or both) retrievals, which could warrant further investigation.

4.2. *Spectral signatures of mineral dust and biomass-burning aerosol*

Figure 5 displays the spectral signature of mineral dust and biomass-burning aerosol typically observed during SAMUM-2. The BTD-spectra were obtained from measured spectra (integrated over the indicated period of time) by subtraction of a simulated clear-sky spectrum in order to reduce the influence of gas absorption effects. All spectra shown were recorded during periods characterized as cloud free by the ground-based LIDAR. We chose to separate the spectra according to the different meteorological phases defined in Knippertz et al. (2011) for the SAMUM-2 campaign: The measurements in Fig. 5 (top panel) were taken during the dust phases 2 (24–26 January) and 3 (28 January–2 February), both included a dust layer at low altitude. In addition, phase 2 is characterized by a lofted smoke layer above the dust, which did not occur during dust phase 3. Dust phase 4 (6–14 February) featured exclusively biomass-burning aerosols accompanied by a marine boundary layer but no dust. For an in-depth analysis of the synoptic situation during the individual phases refer to Knippertz et al. (2011).

We would like to point out the similar shape of all BOA spectra measured during phases 2 and 3 (Fig. 5, top panel), which indicates that the radiative properties of dust aerosol do not change significantly during these two phases. A possible explanation for this observation might be that the dust source regions during both phases were the same. In addition, we would like to stress the similarity of the spectral features in the BOA measurements for the cases not including mineral dust (Fig. 5,

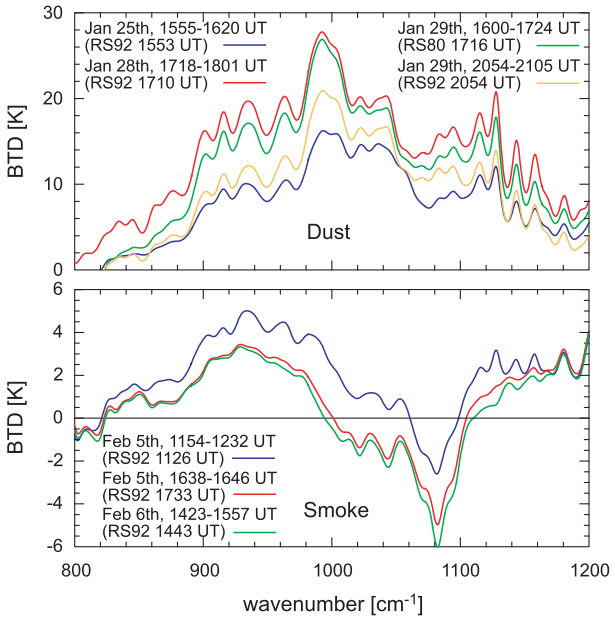

Fig. 5. Dust (top panel) and smoke (bottom panel) signatures recorded at BOA with the D&P Model 102. Both plots show residual BTD obtained by subtracting a simulated clear-sky spectrum from the measured spectra. The labels indicate the time span over which measurements are averaged as well as type and launch time of the radiosonde ingested into the simulation (in brackets).

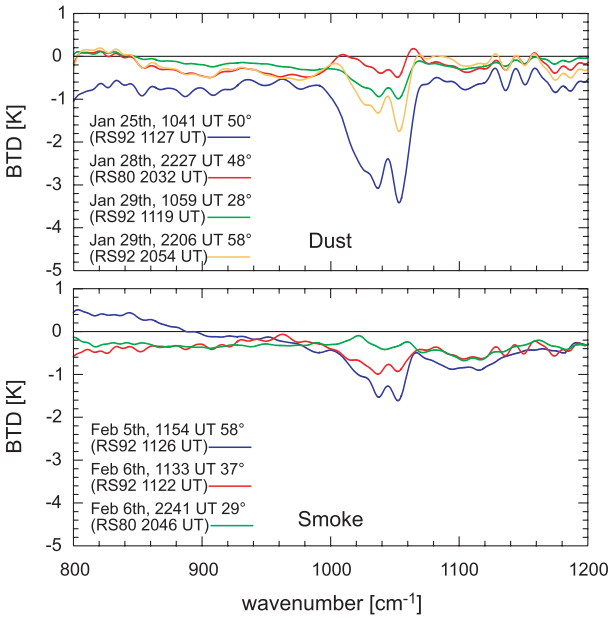

Fig. 6. Dust (top panel) and smoke (bottom panel) signatures recorded at TOA by IASI. Both plots show residual BTD obtained by subtracting a simulated clear-sky spectrum from the measured spectra. The labels indicate time of observation and zenith angle in degree as well as type and launch time of the radiosonde ingested into the simulation (in brackets).

bottom panel) with the assumed instrument bias (see Section 2.2) displayed in Fig. 1 (bottom panel). It it thus probable, that the radiative effect of the lofted biomass-burning aerosol at BOA is smaller than Fig. 5 (bottom panel) would otherwise indicate. The precipitable water column during these cases was very low (26–27 mm), which could lead to an increased influence of the MCT non-linearity compared to the MAERI comparison as discussed in Section 2.2.

Figure 6 is similar to Fig. 5 with the exception that it visualizes the TOA radiative effect of dust and smoke based on IASI observations. It is obvious, that the aerosol effect is far less pronounced at TOA than at BOA, which is to be expected regarding the vertical aerosol structure: the majority of large (dust) particles is located close to the surface in relatively warm layers. Thus it poses a small contrast to the sea surface when observed from TOA, while it is easily discriminated from the cold background when viewed from below. Although it is tempting to attribute the different shapes of the dust signatures on 25 January and 28/29 January to the presence of an additional biomass layer above the dust, it could as well be attributable to the combined uncertainty of measurement and simulation. Comparing Fig. 6 to the sensitivity analysis plotted in Figs. 4a–c one has to conclude, that the aerosol radiative effect caused by dust and smoke at TOA is of the same magnitude as the expected errors, which makes it hard to derive aerosol optical properties from these measurements. In addition, it has to be taken into account that the radiance at TOA will critically depend on the SST, for which no reference measurements at the ground are available. Furthermore many TOA measurements were recorded at relatively high zenith angles of 45° and greater, where the plane-parallel approximation made in the simulations may no longer be valid.

4.3. Case study

In the following section we report on the results of a case study for 25 January. This day is chosen, since almost complete profile information is available, including airborne measurements of aerosol size distributions (Weinzierl et al., 2011) and single aerosol particle analysis (Lieke et al., 2011) at several altitudes. Based on LIDAR observations (Groß et al., 2011; Tesche et al., 2011) we assume a total of four aerosol layers which are summarized in Table 3. In addition to the size distributions of Weinzierl et al. (2011) we assume the ‘dust phase 2’ size distribution of Kandler et al. (2011b) for layer 1. Note that the latter was measured at the ground and contains a high amount of large particles resulting in an increase of the extinction coefficient in the TIR atmospheric window by a factor of 2–3.5 compared to layer 2. This indication of a vertically inhomogeneous mixture is consistent with LIDAR measurements, which also show a substantial increase in the extinction between 0 and 500 m during this day (fig. 2 in Toledano et al., 2011). We compensate for this effect by reducing the vertical extent of layer 1 from 350 m to 200 m.

Table 3. Summary of vertical aerosol layer extension, assumed mineral composition and altitude of size distribution measurement ingested in the column closure for 25 January 2008

Layer ID	Altitude (km)	Aerosol type	Altitude of size dist. meas (km)
1	0–0.2	boundary layer + dust	0.0
2	0.5–1.3	dust	0.8
3	1.5–2.3	smoke + dust	2.0
4	2.5–3.8	smoke + dust	3.5

The boundaries of layers 2–4 were inferred from LIDAR observations while the upper boundary of layer 1, which represents the planetary boundary layer, is derived from radiosonde measurements. The uncertainty of the layer boundaries is estimated to be less than 100 m.

We compare simulated upwelling radiances at TOA with an average over three IASI instantaneous fields of view (IFOVs) recorded at 1041 UT and ingest a radiosonde launched at 1127 UT into our RTM. Modelled downwelling radiances at BOA include radiosonde profiles acquired at 1553 UT and are compared to measurements integrated over the time span 1555–1620 UT. The radiosonde measurements indicate 25 mm and 23 mm of precipitable water at 1127 and 1553 UT, respectively. The aircraft-based observations took place between 1630 and 1650 UT. LIDAR and IASI imager data were evaluated to ensure cloud-free conditions during all radiation measurements. In addition, it has to be taken into account that the time between the IASI overpass and the airborne in situ measurements introduces additional uncertainty, although the LIDAR time series suggest little variation in the vertical aerosol structure during the period in question. Figure 7 displays an overview map including the locations of the measurements accounted for in the case study.

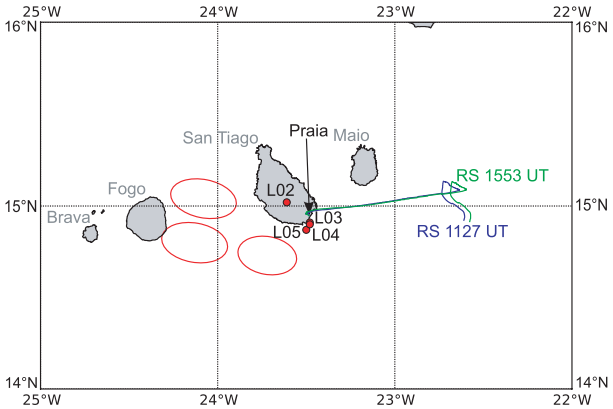

Fig. 7. Geolocation of selected input data used in the case study for 25 January 2008: Circular dots labelled L0x indicate airborne size distribution measurements during flight 080125a. Lines labelled RS are ground tracks of incorporated radiosondes and elliptic shapes indicate IASI footprints (IFOVs).

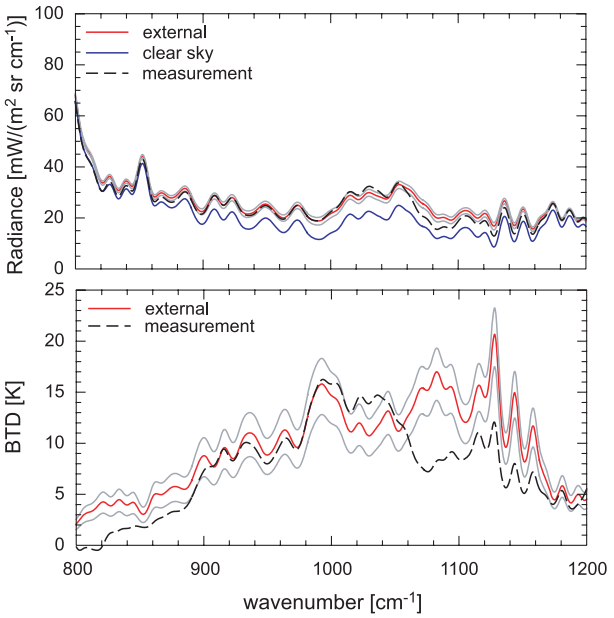

Fig. 8. Comparison of simulated downwelling BOA radiance (solid) using upper and lower envelopes of the size distribution with D&P Model 102 measurement (dashed) for 25 January. The upper panel displays radiances, while the lower panel visualizes BTD obtained through subtraction of a simulated clear-sky spectrum.

Figure 8 shows a comparison of the simulated and measured downwelling radiance at BOA (upper panel) along with a BTD plot of the clear-sky residua (lower panel). The light grey lines are obtained using upper and lower envelopes of the airborne size-distribution measurements for levels 2–4 (no errors were provided with the ground-based measurements) and thus indicate the uncertainty associated with these measurements. Note how deviations between the individual spectra are seemingly enhanced in the BTD plot. Comparing Fig. 8 to the individual uncertainties discussed in Section 4.1 (Fig. 4), the agreement between simulation and measurement is acceptable, although distinct differences between 1050 and 1100 cm^{-1} are observable. These deviations occur in a spectral region, which is most critically affected by the detector non-linearity discussed in Section 2.2, which has been shown to cause an underestimation of the downwelling radiance of up to 5 K in Fig. 1. Furthermore the lower amount of precipitable water encountered during 25 January 2008 could further enhance the bias as discussed earlier. On the other hand we would expect the underestimation to extend over the spectral region from 1000 to 1050 cm^{-1}, too, which is not visible in Fig. 8. In fact, the measured radiance exceeds the simulations here. We will come back to this issue later, after we investigated the influence of several other parameters on the downwelling radiance.

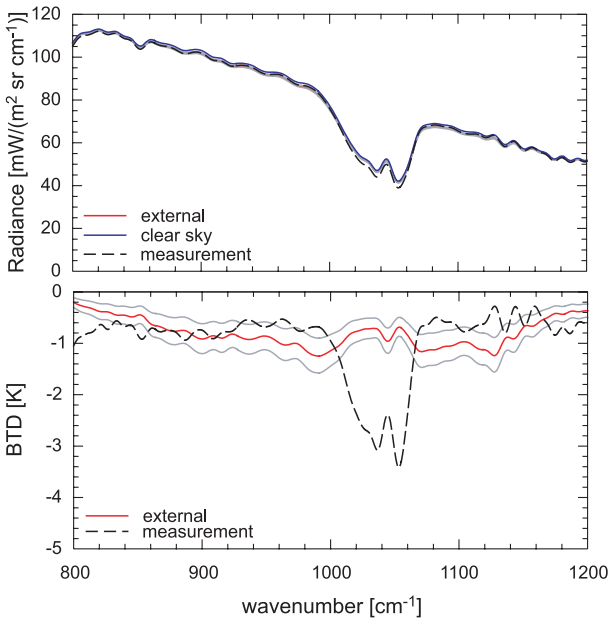

Fig. 9. Comparison of measured (dashed) and simulated upwelling TOA radiance (solid) using upper and lower envelopes of the size distribution for 25 January. The upper panel displays radiances, while the lower panel visualizes BTD obtained through subtraction of the simulated clear-sky spectrum.

As explained in the previous section, we expect the upwelling radiance at TOA to be affected to a lesser extent by the presence of the observed aerosols. This assumption is confirmed by Fig. 9, which displays a comparison of IASI measurements and simulated radiances at TOA similar to the previously discussed Fig. 8. Note that simulated and measured radiances are barely distinguishable, while again differences become more apparent in the BTD plot. The most prominent ones between 1000 and 1070 cm^{-1} are apparently attributable to ozone, as we may infer from Fig. 4a and from the fact, that the retrieved IASI Level 2 ozone column density varies from 262 to 275 DU among the three averaged pixels while the closest GOME-2 measurement yields an ozone column density of 249 DU. For all other parts of the spectrum the observed BTD are well below 1 K and are explainable within the combined uncertainties in water vapour, temperature (Figs 4b and c) and IASI instrument noise (Table 1).

Apart from the size distribution the assumed aerosol refractive index is well known to critically affect the simulated radiances in the TIR (Sokolik et al., 1998). While an external mixture was assumed for the simulations discussed earlier, it is often desirable to model the aerosol with one effective refractive index, since this reduces the necessary number of computations by a factor equalling the number of components included in the mixture. Several ways to proceed are possible, which may be divided up into two groups: models which require the mineral composition as input and models which implicitly assume a composition. Henceforth we will refer to the former as 'microphysical' models and to the latter as 'general' models. Figure 10 (top panels) compares predicted radiances resulting from the application of several refractive index models while the bottom panels are plots of the resulting BTD after subtraction of the clear-sky case. We investigate the microphysical models for external, volumetric and Maxwell-Garnett (1903) effective medium theory (Figs 10a and c) as well as the general Sahara dust models of OPAC (Hess et al., 1998), Shettle and Fenn (1979) and Volz (1973) (Figs 10b and d). The simple volume mixing rule and the Maxwell–Garnett theory perform virtually identical (BTD $\leq$ 0.5 K) over most of the spectrum, while BTD up to 2 K occur around 1100 cm^{-1}. Both seem to predict a higher absorption than the external mixture with pronounced differences in the spectral domain 1080–1130 cm^{-1}, where the BTDs differ by up to 4 K. Overall the external model seems to give a slightly better fit to the measurement than the internal microphysical models. Among the general models, the refractive indices provided by Shettle result in the lowest absorption of all models examined in this study. The OPAC and Volz models agree very well for wavenumbers larger than 1020 cm^{-1}, while the OPAC model predicts more absorption in the wavenumber range 800–900 cm^{-1} and less absorption between 900 and 1000 cm^{-1}.

A similar comparison for the upwelling radiance at TOA is provided by Fig. 11. As before the Maxwell–Garnett and volumetric mixture produce virtually identical results. Interestingly the external mixture causes lower radiances than the internal mixtures in this case, too. Regarding the general mixtures, the picture is essentially the same as at BOA, with very little differences between Volz and OPAC and a generally lower absorption of the Shettle model.

At this point we would like to come back to the uncertainties of surface temperature and emissivity discussed in Section 3.2 and their effect on the simulated radiances at the surface. We found that the uncertainty of the emissivity only accounts for an associated uncertainty of less than 0.2 K in BT at the surface (assuming a surface temperature of 320 K), while a temperature increase of 25 K at the surface caused an increase in downwelling radiance of less than 0.5 K equivalent BT under the assumption of an emissivity of 0.9. Thus it is safe to ignore these uncertainties compared to other possible error sources. Furthermore these findings imply, that aerosol scattering has only a minor effect on the downwelling radiance, since surface emissivity and surface temperature only contribute downwelling radiation through emission and consecutive backscattering. In order to further investigate the issue, we replaced the scattering phase function in each layer by the Henyey and Greenstein (1940) approximation, which is completely determined by the asymmetry parameter. The resulting BTD spectrum obtained after subtraction of the spectrum simulated using the full phase function does not exceed 0.15 K within the TIR atmospheric window. Thus the downwelling TIR radiation seems to be primarily

governed by aerosol absorption and re-emission rather than scattering, although dust single scattering albedos range from 0.4 to 0.75.

We conclude the sensitivity analysis with an examination of the potential errors arising from uncertainties in the vertical aerosol structure. As stated before, we estimate the aerosol layer altitudes to be exact within 100 m. Figure 12 compares the measured spectra with simulations, assuming a vertical upward shift of 100 m for each aerosol layer or by a 100 m increased thickness of each layer. While the vertical shift does not alter the result at all (less than 0.2 K compared to the reference case), the increase of the layer thickness leads to decidedly higher absorption, since the AOD scales linearly with layer vertical extension. A similar effect may be observed at TOA (not shown).

Taking into account all of the above-mentioned potential error sources, the agreement between simulation and observations is satisfactory. However, there still remains an open question regarding the deviations between measured and simulated downwelling radiances in the spectral interval 1050–1100 cm^{-1}. While we cannot completely rule out that these inconsistencies are caused by the detector non-linearity, they would require a strong scene dependence of the associated bias. Furthermore Fig. 10 suggests, that a suitable choice of the refractive index could improve the agreement between model and measurement, since the Volz dust model shows more similarity to the simulations than any of the other dust models. On the other hand, we would expect to achieve a better result using one of the microphysically motivated models, since they include more information regarding the mineral aerosol composition. An examination of the spectral characteristics of the individual mineral refractive indices entering the mixture reveals that many materials, especially silicates and sulphates, exhibit resonance-like features in this spectral region. These so-called reststrahlen bands are characterized by strong absorption and a comparatively small real refractive index (often less than unity). Recent laboratory studies of Hudson et al. (2008) and Mogili et al. (2008) show that the application of the Mie theory in the above-mentioned mineral resonance bands yields absorption peaks, which are shifted towards smaller wavelengths compared to the measured peaks. Mogili et al. (2008) surmised this to originate from the assumption of spherical particles, since simulations using a continuous distribution of spheroids did not display these shifts. Unfortunately their calculations are only applicable in the Rayleigh limit, that is, for particles with diameter considerably smaller than the wavelength of the incident electromagnetic wave, which is not valid in our case. Thomas and Gautier (2009) encountered similar inconsistencies for their IR extinction measurements close to Dakar during a Saharan dust storm, which seemingly agree with the results of Hudson et al. (2008). Note that a shift of

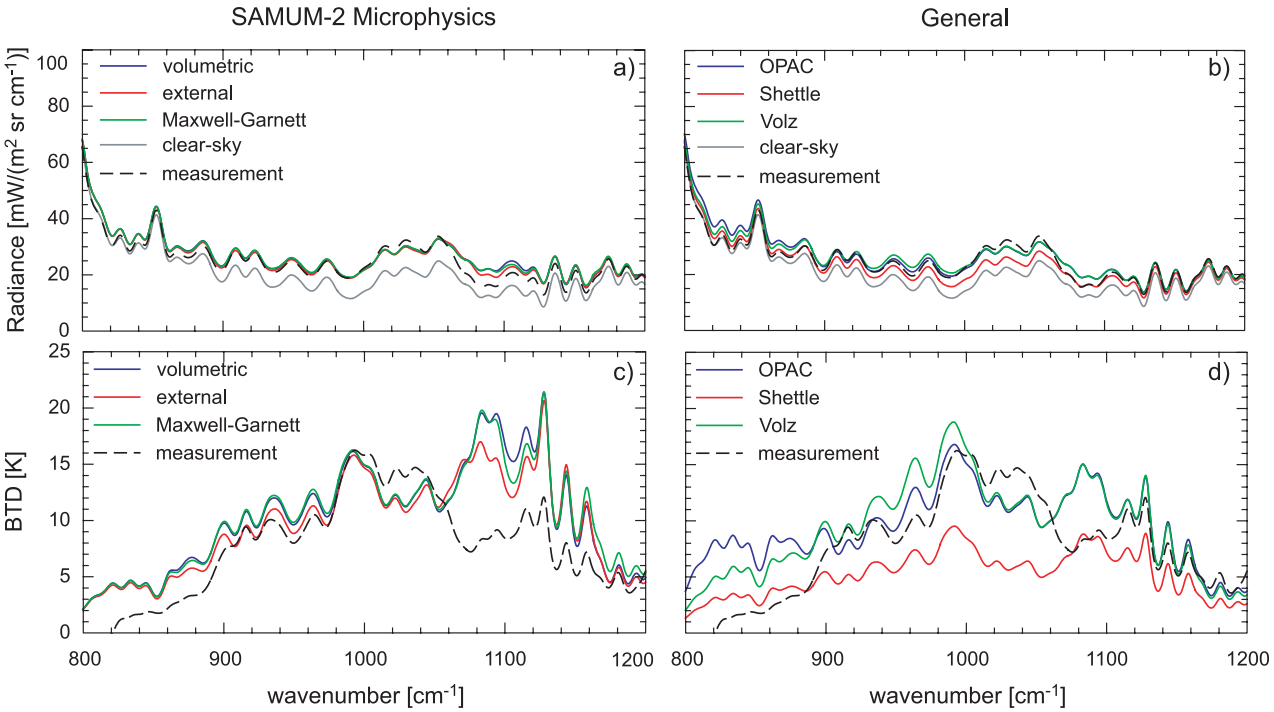

Fig. 10. Comparison of simulated downwelling BOA radiance (solid) using different refractive index models with D&P Model 102 measurement (dashed) for 25 January. Figures a and b display radiances, while Figures c and d show BTD obtained through subtraction of the simulated clear-sky spectrum. The results in the left-hand column account for mineral dust composition measured within the scope of SAMUM-2, while the dust-models plotted in the right-hand column do not require information about aerosol composition.

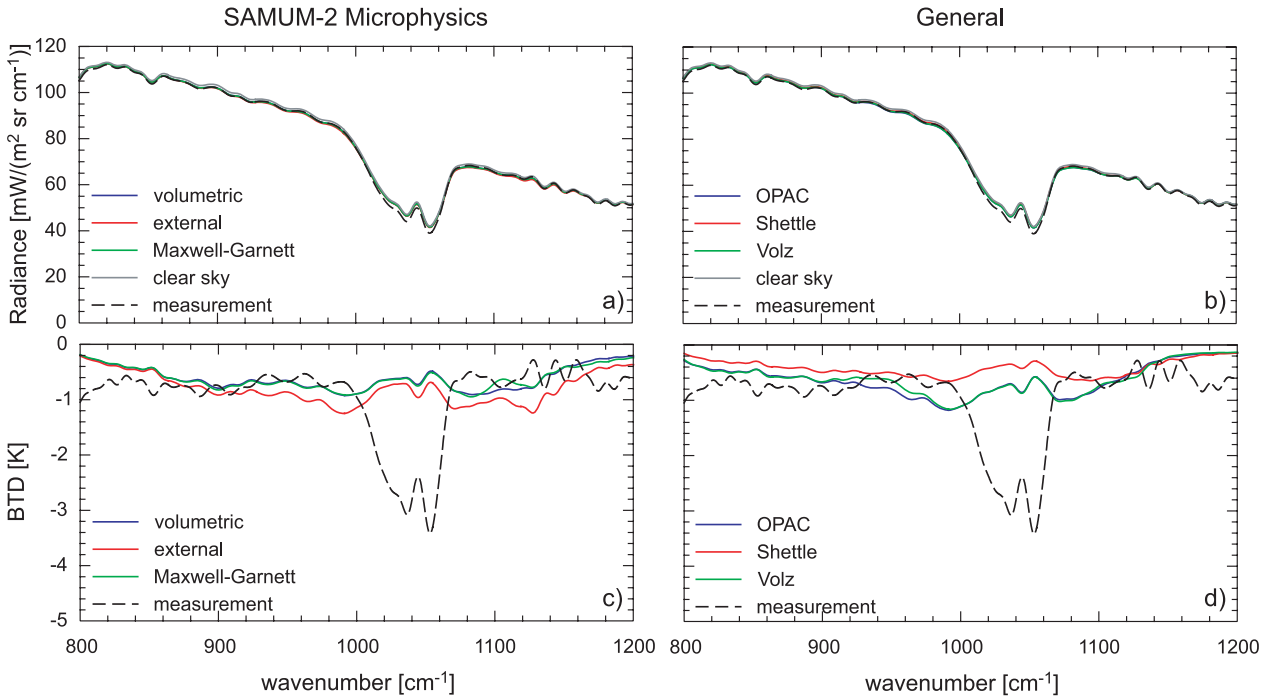

Fig. 11. Comparison of simulated upwelling TOA radiance (solid) using different refractive index models with IASI measurement (dashed) for 25 January. Figures a and b display radiances, while Figures c and d show BTD relative to clear-sky case. The results in the left-hand column account for mineral dust composition measured within the scope of SAMUM-2, while the dust-models plotted in the right column do not require information about aerosol composition.

the simulated absorption peaks in Fig. 8 towards higher wavelengths would cause the simulated radiances to be greater than the measured radiances around 1040 cm^{-1}, resulting in deviations between simulations and measurements comparable to those encountered during the MAERI comparison (see Fig. 1). Anyhow we have to state that the magnitude of the instrument bias and its potential scene-dependence renders the above presented considerations mere speculations. Nonetheless we intend to conduct further investigations regarding the issue.

We would like to close this section with an assessment of the long-wave DRE exerted by the aerosol, which we define in consistency with previous literature for the upwelling (↑) and downwelling (↓) radiation.

$$\Delta F\downarrow = F_{\text{total}}\downarrow - F_{\text{clear}}\downarrow, \tag{5}$$

$$\Delta F\uparrow = F_{\text{clear}}\uparrow - F_{\text{total}}\uparrow, \tag{6}$$

in terms of the (simulated) upwelling flux $F\uparrow$ at BOA integrated over the TIR atmospheric window and its downwelling counterpart $F\downarrow$ at TOA. In both equations the subscript 'clear' denotes a simulation for the clear-sky case. The resulting values for the DRE are summarized in Table 4 for the different scenarios discussed previously. It should be noted, that all quantities were calculated for 1124 UT to allow for a consistent comparison of DRE at TOA and BOA, although our studies imply that the difference in DRE between simulations for 1124 UT and 1553 UT never exceed 1 W m^{-2}. As can be inferred from Table 4, the different refractive index models have a minor effect on the DRE, except for the Shettle model, which seemingly underestimates the radiation, especially at BOA. Overall the uncertainties in size distribution seem to outweigh those in refractive index. Furthermore note the large differences in DRE at BOA and TOA. These are due to the fact, that the optically thick aerosol layers are close to the surface and thus show little contrast compared to the ground when regarded from TOA. Conversely their contrast towards the cold background when observed from BOA makes for a large DRE at the surface.

5. Summary and outlook

Ground-based FTIR measurements have been proven to be very sensitive to the presence of mineral dust at low altitudes as customarily observable in the tropical Atlantic during the winter month. Despite an instrument bias, which could not be corrected, a distinct radiative effect caused by a combination of mineral dust and biomass-burning aerosol has been isolated in the spectral region from 800 to 1200 cm^{-1}. We have shown, that the aerosol's radiative effect in the TIR is dominated by the large mineral dust particles, whereas the biomass burning aerosol seems to have a negligible effect. An evaluation of IASI measurements revealed

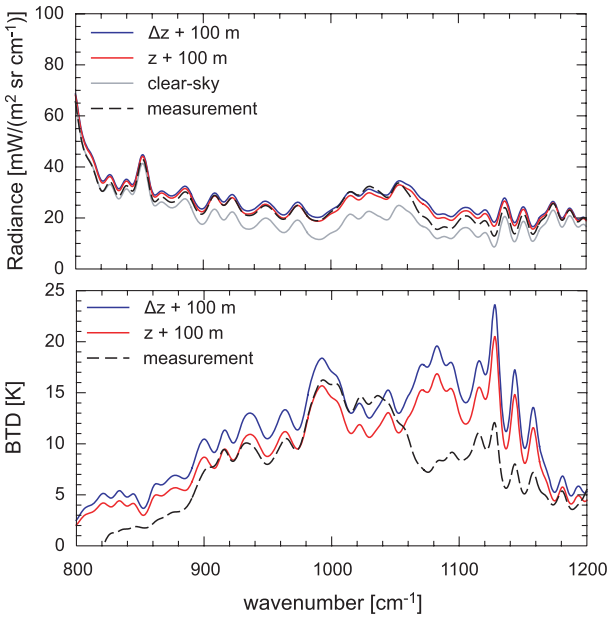

Fig. 12. Comparison of measured (dashed) and simulated downwelling BOA radiance (solid) obtained after shifting all aerosol layers 100 m upwards ($\Delta z + 100$ m) and by increasing the vertical extension of each aerosol layer by 100 m ($z + 100$ m). The upper panel displays radiances, while the lower panel visualizes BTD obtained through subtraction of the simulated clear-sky spectrum.

that the aerosol's radiative effect is much more pronounced at BOA compared to TOA due to the low altitude of the optically thick dust-dominated layers. Thus the uncertainties in relative humidity, temperature and ozone profile are too large to extract detailed information on the aerosols radiative properties from TOA measurements in this case.

The case study performed for 25 January 2008, a day characterized by high dust loads at low altitudes, which were superseded by lofted biomass-burning aerosol layers, shows that simulated radiances at BOA and TOA agree within their respective error budgets with measured radiances. Taking a closer look at the sensitivity of the simulated radiances towards uncertainties in the input parameters, it can be observed that small modifications of aerosol size distribution or vertical aerosol distribution cause changes in magnitude of the aerosol's radiative impact but hardly alter its spectral signature. In contrast to that, changes in the refractive index model have the potential to modify the dust spectral signature. Among the microphysically motivated refractive index models (volumetric mixture, Maxwell–Garnett effective medium theory and external mixture) the most prominent differences were constrained to a small spectral region from 1070 to 1100 cm^{-1} with a maximum of deviation of 4 K in equivalent brightness temperature. For the rest of the spectral domain the agreement of these models was better than 2 K. The dust models of Volz and OPAC produce very similar results and are almost identical between 1000 and 1200 cm^{-1}, while the Shettle

Table 4. Simulated DRE for 25 January 2008 (precipitable water vapour 25 mm)

	DRE (W m^{-2})	
Scenario	BOA	TOA
Reference	8.7	1.0
Size dist −	6.7	0.6
Size dist +	10.4	1.4
External	8.0	1.3
$\Delta z + 100$ m	9.6	1.5
Maxwell–Garnett	8.7	1.0
OPAC	8.1	1.0
Shettle	4.0	0.7
Volz	8.0	1.0
Land surface	9.1	2.9

Note: All cases are for a sea surface at 295 K except for 'land surface', which assumes an emissivity of 0.9 and a temperature of 315 K at BOA. 'Size dist −'/'Size dist +' designate the values obtained with the lower/upper envelopes of the size distributions and '$\Delta z + 100$m' refers to a 100m increase in vertical extension of each aerosol layer.

dust model seemingly underestimates the dust radiative impact. Beyond this the instrument bias, which is largest in the spectral region where the individual models differ most, prohibits the preference of one model over the other, although the Volz model produces a slightly better fit to our measurements compared to the other models. This seems surprising, since this specific model does not include any information on the mineral composition of the aerosol. Unfortunately, the question whether the comparatively poorer performance of the microphysical models is attributable to instrument bias, errors in the assumed mineral composition or disregard of particle non-sphericity cannot be ultimately answered. Nonetheless our findings warrant further investigation of the issue in the light of recent experimental results, which seemingly contradict earlier studies suggesting that Mie theory was an adequate tool to model the radiative properties of mineral dust aerosol in the TIR.

Regarding the DRE of the aerosol mixture it has to be stated, that the above-mentioned issues have relatively little effect compared to uncertainties in size distribution or vertical layering. The values of 8 W m^{-2} at BOA and 1 W m^{-2} at TOA over the ocean are in agreement with earlier studies (and references therein Hansell et al., 2010).

We believe that ground-based radiance measurements as described in this paper provide valuable insight into instrument performance and modelling capabilities of current aerosol and RTMs. The combination of in situ observations and high-precision radiation measurements should be intensified to validate existing benchmark aerosol models and test the errors caused by common approximations, for example, the application of Mie theory to non-spherical dust particles. The TIR seems to be especially suited for this task, since the aerosol particles

have smaller size parameters compared to the UV/VIS, which greatly simplifies the simulations of the aerosol single scattering properties. We believe that a better understanding of aerosol optical properties is a pre-requisite to advance the capabilities of ground-based, airborne and space-borne retrieval of aerosol concentration and aerosol microphysical properties, which are needed to monitor and predict weather and climate on the Earth.

6. Acknowledgments

We are indebted to Colonel Antonio Fortes for his invaluable support during the SAMUM-2 field campaign. Furthermore we would like to thank Volker Tank for organizational support and the DLR flight operations department for transporting our equipment and providing excellent catering service. In addition, we are very grateful for the support we received from Stuart Newman and Alan Vance during our visit to Exeter and we would like to express our gratitude to the staff of D&P instruments, who supported us in our efforts with the Model 102. This study was supported by the German Research Foundation (DFG) within the Research Group SAMUM under grant FOR 539.

References

Ansmann, A., Petzold, A., Kandler, K., Tegen, I., Wendisch, M. and co-authors. 2011. Saharan Mineral Dust Experiments SAMUM-1 and SAMUM-2: what have we learned? *Tellus* **63B**, this issue.

Aronson, J. R. 1986. Optical constants of monoclinic anisotropic crystals: orthoclase. *Spectrochimica Acta* **42A**(2/3), 187–190.

Aronson, J. R. and Strong, P. F. 1975. Optical constants of minerals and rocks. *Appl. Opt.* **14**(12), 2914–2920.

Bertie, J. E. and Lan, Z. 1996. Infrared intensities of liquids XX: the intensity of the OH stretching band of liquid water revisited, and the best current values of the optical constants of H_2O(l) at 25 °C between 15,000 and 1 cm^{-1}. *Appl. Spectrosc.* **50**(8), 1047–1057.

Bharmal, N. A., Slingo, A., Robinson, G. J. and Settle, J. J. 2009. Simulation of surface and top of atmosphere thermal fluxes and radiances from the radiative atmospheric divergence using the ARM mobile facility, GERB data, and AMMA stations experiment. *J. Geophys. Res.* **114**, D00E07. doi:10.1029/2008JD010504.

Cady-Pereira, K. E., Shephard, M. W., Turner, D. D., Mlawer, E. J., Clough, S. A. and co-authors. 2008. Improved daytime column-integrated precipitable water vapor from Vaisala Radiosonde Humidity Sensors. *jaot* **25**, 873–883.

Clough, S., Shephard, M., Mlawer, E., Delamere, J., Iacono, M. and co-authors. 2005. Atmospheric radiative transfer modeling: a summary of the AER codes. *J. Quant. Spectrosc. Radiat. Transfer* **91**(2), 233–244. doi:10.1016/j.jqsrt.2004.05.058.

Fiedler, L., Newman, S. and Bakan, S. 2005. Correction of detector nonlinearity in Fourier transform spectroscopy with a low-temperature blackbody. *Appl. Opt.* **44**(25), 5332–5340.

Friedman, D. 1969. Infrared characteristics of ocean water (1.5-15 μm). *Appl. Opt.* **8**, 2073–2078.

Glotch, T. D., Christensen, P. R. and Sharp, T. G. 2006. Fresnel modeling of hematite crystal surfaces and application to martian hematite spherules. *Icarus* **181**, 408–418.

Glotch, T. D., Rossman, G. R. and Aharonson, O. 2007. Mid IR reflectance spectra and optical constants of ten phyllosilicate minerals. *Icarus* **192**, 605–622.

Groβ, S., Gasteiger, J., Freudenthaler, V., Wiegner, M., Greiß, A. and co-authors. 2011. Characterization of the planetary boundary layer during SAMUM-2 by means of lidar measurements. *Tellus* **63B**, this issue.

Hansell, R. A., Liou, K. N., Ou, S. C., Tsay, S. C., Ji, Q. and co-authors. 2008. Remote sensing of mineral dust aerosol using AERI during the UAE^2: a modeling and sensitivity study. *J. Geophys. Res.* **113**, 18202–+. doi:10.1029/2008JD010246.

Hansell, R. A., Tsay, S. C., Ji, Q., Hsu, N. C., Jeong, M. J. and co-authors. 2010. An assessment of the surface longwave direct radiative effect of airborne saharan dust during the NAMMA field campaign. *J. Atmos. Sci.* **67**(4), 1048–1065. doi:10.1175/2009JAS3257.1.

Henning, T. and Mutschke, H. 1997. Low-temperature IR properties of cosmic dust analogues. *Astron. Astrophys.* **327**, 743–754.

Henyey, L. G. and Greenstein, J. L. 1940. Diffuse radiation in the Galaxy. *Annales d'Astrophysique* **3**, 117–137.

Hess, M., Koepke, P. and Schult, I. 1998. Optical properties of aerosols and clouds: the software package OPAC. *Bull. Am. Met. Soc.* **79**, 831–844.

Highwood, E. J., Haywood, J. M., Silverstone, M. D., Newman, S. M. and Taylor, J. P. 2003. Radiative properties and direct effect of Saharan dust measured by the C-130 aircraft during Saharan Dust Experiment (SHADE): 2. Terrestrial spectrum. *J. Geophys. Res.* **108**(D18), 8578. doi:10.1029/2002JD002552.

Hoidale, G. B. and Blanco, A. J. 1969. Infrared absorption spectra of atmospheric dust over an interior desert basin. *Pure Appl. Geophys.* **74**(1), 151–164. 10.1007/BF00875195. doi:10.1007/BF00875195.

Hollweg, H., Bakan, S. and Taylor, J. P. 2006. Is the aerosol emission detectable in the thermal infrared? *J. Geophys. Res.* **111**, D15202. doi:10.1029/2005JD006432.

Hudson, P. K., Gibson, E. R., Young, M. A., Kleiber, P. D. and Grassian, V. H. 2008. Coupled infrared extinction and size distribution measurements for several clay components of mineral dust aerosol. *J. Geophys. Res.* **113**, D01201. doi:10.1029/2007JD008791.

Kandler, K., Lieke, K., Benker, N., Emmel, C., Kuepper, M. and co-authors. 2011a. Electron microscopy of particles collected at Praia, Cape Verde, during the Saharan Mineral dust experiment: particle chemistry, shape, mixing state and complex refractive index. *Tellus* **63B**, this issue.

Kandler, K., Schütz, L., Jaeckel, S., Lieke, K., Emmel, C. and co-authors. 2011b. Ground-based off-line aerosol measurements at Praia, Cape Verde, during the Saharan Mineral Dust Experiment: microphysical properties and mineralogy. *Tellus* **63B**, this issue.

Kleinert, A., Aubertin, G., Perron, G., Birk, M., Wagner, G. and co-authors. 2007. MIPAS Level 1B algorithms overview: operational processing and characterization. *Atmos. Chem. Phys.* **7**(5), 1395–1406.

Knippertz, P., Tesche, M., Heinold, B., Kandler, K., Toledano, C. and co-authors. 2011. Dust mobilization and aerosol transport from Western Africa to Cape Verde: a meteorological overview of SAMUM-2. *Tellus* **63B**, this issue.

Knuteson, R. O., Revercomb, H. E., Best, F. A., Ciganovich, N. C., Dedecker, R. G. and co-authors. 2004a. Atmospheric emitted radiance interferometer, part I: instrument design. *J. Atmos. Ocean. Technol.* **21**(12), 1763–1776. doi:10.1175/JTECH-1662.1.

Knuteson, R. O., Revercomb, H. E., Best, F. A., Ciganovich, N. C., Dedecker, R. G. and co-authors. 2004b. Atmospheric emitted radiance interferometer, part II: instrument performance. *J. Atmos. Ocean. Technol.* **21**(12), 1777–1789. doi:10.1175/JTECH-1663.1.

Koehler, C. H., Trautmann, T. and Lindermeir, E. 2009. Measurement of mixed biomass burning and mineral dust aerosol in the thermal infrared. *AIP Conference Proceedings* **1100**(1), 169–172. doi:10.1063/1.3116940.

Korb, A. R., Dybward, P., Wadsworth, W. and Salisbury, J. 1996. Portable Fourier transform infrared spectroradiometer for field measurements of radiance and emissivity. *Appl. Opt.* **35**(10), 1679–1692.

Kuntz, M. and Hoepfner, M. 1999. Efficient line-by-line calculation of absorption coefficients. *J. Quant. Spectrosc. Radiat. Transfer* **63**(1), 97–114. doi:10.1016/S0022-4073(98)00140-X.

Lieke, K., Kandler, K., Scheuvens, D., Emmel, C., von Glahn, C. and co-authors. 2011. Particle chemical properties in the vertical column based on aircraft observations in the vicinity of Cape Verde Islands. *Tellus* **63B**, this issue.

Lindermeir, E., Haschberger, P., Tank, V. and Dietl, H. 1992. Calibration of a Fourier transform spectrometer using three blackbody sources. *Appl. Opt.* **31**(22), 4527–4533. doi:10.1364/AO.31.004527.

Long, L. L., Querry, M. R., Bell, R. J. and Alexander, R. W. 1993. Optical properties of calcite and gypsum in crystallinte and powdered form in TIR and FIR. *Infrared Phys.* **34**(2), 191–201.

Loyola, D., Koukouli, M., Valks, P., Balis, D., Hao, N. and co-authors. 2011. The GOME-2 total column ozone product: retrieval algorithm and ground-based validation. *J. Geophys. Res.* **116**, D07302, doi:10.1029/2010JD014691, in press.

Maxwell-Garnett, J. C. 1903. Colours in metal glasses and in metallic films. *Philos. Trans. R. Soc. A*} **203**, 385–420.

Mayer, B. and Kylling, A. 2005. Technical note: the libRadtran software package for radiative transfer calculations, description and examples of use. *Atmos. Chem. Phys.* **5**(7), 1855–1877. doi:10.5194/acp-5-1855-2005.

Minnett, P. J., Knuteson, R. O., Best, F. A., Osborne, B. J., Hanafin, J. A. and co-authors. 2001. The marine-atmospheric emitted radiance interferometer: a high-accuracy, seagoing infrared spectroradiometer. *J. Atmos. Ocean. Technol.* **18**(6), 994–1013. doi:10.1175/1520-0426(2001)018<0994:TMAERI>2.0.CO;2.

Mogili, P. K., Yang, K. H., Young, M. A., Kleiber, P. D. and Grassian, V. H. 2008. Extinction spectra of mineral dust aerosol components in an environmental aerosol chamber: IR resonance studies. *Atmos. Environ.* **42**, 1752–1761.

Mooney, T. and Knacke, R. F. 1985. Optical constants of chlorite and serpentine between 2.5 and 50 μm. *Icarus* **64**, 493–502.

Mutschke, H., Begemann, B., Dorschner, J., Guertler, J., Gustafson, B. and co-authors. 1998. Steps toward interstellar silicate mineralogy, III: the role of aluminium in circumstellar amorphous silicates. *Astron. Astrophys.* **333**, 188–198.

Nousiainen, T. 2009. Optical modeling of mineral dust particles: a review. *J. Quant. Spectrosc. Radiat. Transfer* **110**(14-16), 1261–1279. XI Conference on Electromagnetic and Light Scattering by Non-Spherical Particles: 2008. doi:10.1016/j.jqsrt.2009.03.002.

Oreopoulos, L. and Mlawer, E. 2010. The continual intercomparison of radiation codes (CIRC). *Bull. Am. Met. Soc.* **93**(3), 305–310.

Otto, S., Bierwirth, E., Weinzierl, B., Kandler, K., Esselborn, M. and co-authors. 2009. Solar radiative effects of a Saharan dust plume observed during SAMUM assuming spheroidal model particles. *Tellus* **61B**, 270–296. doi:10.1111/j.1600-0889.2008.00389.x.

Querry, M. R., Osborne, G., Lies, K., Jordon, R. and Coveney, R. M. 1978. Complex refractive index of limestone in the visible and infrared. *Appl. Opt.* **17**(3), 353–356.

Revercomb, H. E., Buijs, H., Howell, H. B., LaPorte, D. D., Smith, W. L. and co-authors. 1988. Radiometric calibration of IR fourier transform spectrometers: solution to a problem with the high-resolution interferometer sounder. *Appl. Opt.* **27**(15), 3210–3218.

Rother, T., Ed. 2009. *Electromagnetic Wave Scattering on Nonspherical Particles: Basic Methodology and Simulations*. Springer-Verlag GmbH, Heidelberg. ISBN 9783642007033.

Rothman, L., Gordon, I., Barbe, A., Benner, D., Bernath, P. and co-authors. 2009. The hitran 2008 molecular spectroscopic database. *J. Quant. Spectrosc. Radiat. Transfer* **110**(9-10), 533–572. doi:10.1016/j.jqsrt.2009.02.013.

Schmidt, K., Wauer, J., Rother, T. and Trautmann, T. 2009. Scattering database for spheroidal particles. *Appl. Opt.* **48**(11), 2154–2164.

Shettle, E. P. and Fenn, R. W. 1979. Models for the Aerosols of the lower atmosphere and the effects of humidity variations on their optical properties, technical report AFGL-TR-79-0214, AFGL.

Sokolik, I. 2002. The spectral radiative signature of wind-blown mineral dust: implications for remote sensing in the thermal IR region. *Geophys. Res. Lett.* **29**(24), 2154. doi:10.1029/2002GL015910.

Sokolik, I., Toon, O. B. and Bergstrom, R. W. 1998. Modeling the radiative characteristics of airborne mineral aerosols at infrared wavelenghts. *J. Geophys. Res.* **103**, 8813–8826. doi:10.1029/98JD00049.

Stamnes, K., Tsay, S., Jayaweera, K. and Wiscombe, W. 1988. Numerically stable algorithm for discrete-ordinate-method radiative transfer in multiple scattering and emitting layered media. *Appl. Opt.* **27**, 2502–2509.

Sutherland, R. A. and Khanna, R. K. 1991. Optical properties of organic-based aerosols produced by burning vegetation. *Aerosol. Sci. Technol.* **14**, 331–342.

Tesche, M., Gross, S., Ansmann, A., Müller, D., Althausen, D. and co-authors. 2011. Profiling of Saharan dust and biomass burning smoke with multiwavelength polarization Raman lidar at Cape Verde. *Tellus* **63B**, this issue.

Thomas, M. and Gautier, C. 2009. Investigations of the March 2006 African dust storm using ground-based column-integrated high spectral resolution infrared (8-13 μm) and visible aerosol optical thickness measurements: 2. Mineral aerosol mixture analyses. *J. Geophys. Res.* **114**, D14209. doi:10.1029/2008JD010931.

Toledano, C., Wiegner, M., Groß, S., Freudenthaler, V., Gasteiger, J. and co-authors. 2011. Optical properties of aerosol mixtures derived from sun-sky radiometry during SAMUM-2. *Tellus* **63B**, this issue.

Toon, O. B., Pollock, J. B. and Khare, B. N. 1976. The optical constants of several atmospheric aerosols species: ammonium sulfate, aluminum oxide and sodium chloride. *J. Geophys. Res.* **81**, 5733–5748.

Turner, D. D. 2008. Ground-based infrared retrievals of optical depth, effective radius, and composition of airborne mineral dust above the Sahel. *J. Geophys. Res.* **113**, D00E03. doi:10.1029/2008JD010054.

Volz, F. E. 1973. Infrared optical constants of ammonium sulfate, Sahara dust, volcanic pumice, and flyash. *Appl. Opt.* **12**, 564–568.

Vömel, H., Selkirk, H., Miloshevich, L., Valverde-Canossa, J., Valdes, J. and co-authors. 2007. Radiation dry bias of the Vaisala RS92 humidity sensor. *J. Atmos. Ocean. Technol.* **24**, 953–963.

Weinzierl, B., Sauer, D., Esselborn, M., Petzold, A., Veira, A. and co-authors. 2011. Microphysical and optical properties of dust and tropical biomass burning aerosol layers in the Cape Verde region: an overview of the airborne in-situ and lidar measurements during SAMUM-2. *Tellus* **63B**, this issue.

Wiscombe, W. J. 1980. Improved Mie scattering algorithms. *Appl. Opt.* **19**(9), 1505–1509.